

THE DYNAMICAL STATE OF THE GLOBULAR CLUSTER M 10 (NGC 6254)

G. BECCARI¹, M. PASQUATO², G. DE MARCHI¹, E. DALESSANDRO³, M. TRENTI⁴, M. GILL⁵

Accepted for publication in "The Astrophysical Journal"

ABSTRACT

Studying the radial variation of the stellar mass function in globular clusters (GCs) has proved a valuable tool to explore the collisional dynamics leading to mass segregation and core collapse. Recently, Pasquato et al. (2009) used the mass segregation profile to investigate the presence of an intermediate-mass black hole (IMBH) in NGC 2298. As a relaxed cluster with a large core, M 10 (NGC 6254) is suitable for a similar investigation. In order to study the radial dependence of the luminosity and mass function of M 10, we used deep high resolution archival images obtained with the Advanced Camera for Survey (ACS) on board the Hubble Space Telescope (HST), reaching out to approximately the cluster's half-mass radius (r_{hm}), combined with deep Wide Field and Planetary Camera 2 (WFPC2) images that extend our radial coverage to more than $2r_{hm}$. From our photometry, we derived a radial mass segregation profile and a global mass function that we compared with those of simulated clusters containing different energy sources (namely hard binaries and/or an IMBH) able to halt core collapse and to quench mass segregation. A set of direct N-body simulations of GCs, with and without an IMBH of mass 1% of the total cluster mass, comprising different initial mass functions (IMFs) and primordial binary fractions, was used to predict the observed mass segregation profile and mass function.

The mass segregation profile of M 10 is not compatible with cluster models without either an IMBH or primordial binaries, as a source of energy appears to be moderately quenching mass segregation in the cluster. Unfortunately, the present observational uncertainty on the binary fraction in M 10 does not allow us to confirm the presence of an IMBH in the cluster, since an IMBH, a dynamically non-negligible binary fraction ($\sim 5\%$), or both can equally well explain the radial dependence of the cluster mass function.

Subject headings: globular clusters: general — globular clusters: individual(M 10) — stars: luminosity function, mass function

1. INTRODUCTION

Globular Clusters (GCs) are important astrophysical laboratories for the study of both stellar evolution and stellar dynamics. In recent years it has become clear that these two astrophysical processes cannot be studied independently: physical interactions between single stars as well as the formation, evolution, survival and interactions of binary systems have a significant role in the evolution of the clusters and of their stellar populations (Spitzer 1987). Such interactions change the energy budget of the cluster and therefore influence the time scales on which mass segregation, core collapse and other dynamical processes occur. On the evolutionary side, they can generate objects that cannot be explained by standard stellar evolution (like blue stragglers, X-ray binaries, millisecond pulsars, etc.; see Ferraro 2006, and references therein).

Recently, various clues have emerged that point to the presence of intermediate-mass black holes (IMBHs) in GCs. On the theoretical side at least three different formation mechanisms have been proposed, namely merging of stellar-mass black holes via four-body interactions (Miller & Hamilton 2002), runaway merging of massive stars (Portegies Zwart et al. 2004), and the death of Pop III stars in the early universe, which would leave IMBHs behind as

remnants, as shown e.g. by Madau & Rees (2001) (see also Trenti & Stiavelli 2007a). Detailed collisional N-body simulations (Baumgardt et al. 2005; Trenti et al. 2007b) and theoretical arguments (Heggie et al. 2007) have shown that an IMBH can be at the origin of a shallow central cusp in the surface brightness profile (SBP) of GCs that have been observed in the projected density profile of a few GCs by Noyola & Gebhardt (2006, 2007), Lanzoni et al. (2007), and Ibata et al. (2009).

Line-of-sight velocity studies were undertaken by Baumgardt et al. (2003a), van den Bosch et al. (2006), and Chakrabarty (2006) on M 15, by Gebhardt et al. (2002), Baumgardt et al. (2003b), Gebhardt et al. (2005) on G 1, by Noyola et al. (2008), Anderson & van der Marel (2009), Sollima et al. (2009) on ω Cen, resulting for now in no undisputed definitive detection. Ibata et al. (2009) recently found a stellar density cusp and a velocity dispersion increase in the center of the globular cluster M 54. This could be explained by the presence of a $\sim 9400M_{\odot}$ black hole if the cusp stars possess moderate radial anisotropy. Proper motion studies from Hubble Space Telescope (HST) data are likely the best way to attack the problem, but they are technologically challenging and inherently time-consuming, requiring multi-epoch HST-quality observations.

Numerical simulations by Baumgardt et al. (2004) have shown that IMBHs produce a clear photometric signature in GCs, in terms of a large core to half-mass-radius ratio. Moreover, Gill et al. (2008) show that a quenching of mass segregation is predicted by N-body simulations of clusters harboring an IMBH, resulting in an observable signature on the radial dependence of the stellar mass function in GCs, which can be used to either suggest or rule out the presence of an

¹ ESA, Space Science Department, Keplerlaan 1, 2200 AG Noordwijk, The Netherlands, gbeccari@rssi.esa.int

² Department of Physics, University of Pisa, Largo Bruno Pontecorvo 3, I-56127, Pisa, Italy.

³ Department of Astronomy, University of Bologna, Ranzani 1, I-40127, Bologna, Italy.

⁴ Center for Astrophysics and Space Astronomy, University of Colorado, Boulder, CO, 80309-0389 USA.

⁵ Department of Astronomy, University of Maryland, College Park, MD 20742-2421

IMBH. Pasquato et al. (2009) provide the first application of this method, using the observed mass segregation profile to argue against the presence of an IMBH in NGC 2298. More generally, studying the radial dependence of the stellar mass function in collisionally relaxed GCs can lead to valuable insights on the underlying dynamics of the relaxation processes, such as stellar evaporation, mass segregation and core collapse.

Mass segregation occurs in star clusters as two-body relaxation processes drive the system towards energy equipartition. Heavier stars sink towards the center of the cluster, while the lighter stars preferentially live in the outer regions and are more likely to attain escape velocity from the system. If an additional energy source is present, such as a dynamically significant population of binaries or an IMBH, the mass segregation and the core collapse processes are slowed down and the arising gradient of the IMF is less steep. Also a significant population of stellar mass black holes can in principle segregate in the center of the cluster and sustain a large core (see Mackey et al. 2008), thereby acting as an energy source. This effect is observed in our N-BODY simulations with a Salpeter (1955) IMF (see Section 5), which produces comparatively more remnants than a Miller & Scalo (1979) IMF. However, in such simulations this effect typically lasts a few Gyr, because stellar mass black holes kick each other out of the system via dynamical interactions, and is therefore unlikely to be at work in M 10, which is approximately 11.8 ± 1.1 Gyr old (Salaris & Weiss 2002). In any case, a Salpeter (1955) IMF likely overestimate the number of large stellar-mass black holes produced in a real GC, so any effect of such a *dark core* on the long-term dynamics of the cluster is effectively ruled out.

IMBHs and binaries both work towards reducing the degree of mass segregation attained by a GC at a given (dynamical) age. A realistic binary fraction can partly mimic the effects of an IMBH, so a detailed knowledge of the binary fraction allows more robust conclusions either in favor or against the presence of an IMBH. So far, however, only for a few GCs has a reliable binary fraction been estimated with robust photometric methods based on main sequence (MS) broadening (see Sollima et al. 2007; Milone et al. 2008, and references therein), so the type of study that we discuss here is only possible for a handful of clusters.

M 10 is a reasonable candidate for harboring an IMBH since it displays a ratio of almost 0.4 (McLaughlin & van der Marel 2005) between the core radius and the half-light radius, which in dynamically old clusters is usually interpreted as the signature of an extra energy source (see Vesperini & Chernoff 1994). In addition, M10 is an ideal candidate for the mass segregation method described and employed for NGC2298 by Pasquato et al. (2009) because, with a mass of about $1.5 \times 10^5 M_{\odot}$ (McLaughlin & van der Marel 2005), it is dynamically relaxed ($\log(t_h) = 8.86 \text{ yrs}$; Harris 1996) and has not been overly influenced by the Galactic tidal field ($r_t/r_{hm} = 11.86$ and $R_{gc} = 4.6$ kpc; Harris 1996). These conditions ensure that it has experienced many initial half-mass relaxation times and thus has achieved equilibrium with respect to mass segregation.

The structure of the paper is as follows. We present the data analysis in Sect. 2 and the resulting color-magnitude diagram of M 10 Sect. 2.2. The radial dependence of the mass and luminosity function is showed in Sect. 3, while in Sect. 4 the global mass function (GMF) of the cluster is derived. In

TABLE 1
OBSERVATIONS

Camera	Filter	#exp.	Exp. Time
ACS	F606W	4	90s
-	F814W	4	90s
WFPC2	F606W	1	1100s
-	F606W	3	1200s
-	F814W	1	1100s
-	F814W	3	1200s

Sect. 5 we compare the observed mass segregation profile with predictions from our N-body simulations. A summary and conclusions follow in Sect. 6.

2. OBSERVATIONS AND ANALYSIS

The photometric data used here consist of two main data sets. The ‘‘ACS sample’’ consists of a set of HST images of the core region obtained with the Advanced Camera for Survey (ACS) through the F606W and F816W filters (GO-10775; P.I.: A. Sarajedini; see Table 1). The ACS Wide Field Channel (WFC), employs a mosaic of two 4096×2048 pixels CCD, providing a plate-scale of $0''.05/\text{pixel}$ and a total field of view (FOV) of $3'.4 \times 3'.4$. The dithering pattern used in the observations allows us to sample cluster stars from the very center out to the nominal half-mass radius ($r_h \sim 1'.81$; Harris et al. (1996)). Since we were interested in deriving accurate photometry of the cluster’s low-mass MS population ($M \leq 0.3M_{\odot}$), we retrieved from the ESO/ST-ECF Science Archives only images with long exposure times ($t_{\text{exp}} = 90$ s). All the flat-fielded images (FLT) were properly corrected for geometric distortions and for the effective area of each pixel, following the prescriptions of Sirianni et al. (2005).

The ‘‘WFPC2 sample’’ consists of a series of deep HST images obtained with the F606W and F814W filters of the Wide Field Planetary Camera 2 (WFPC2) on 1995, September 30 during Cycle 5 (Prop.: 6113; P.I.: Paresce). A description of the number of exposures and their duration is given in Table 1. The WFPC2 field is located about $3'$ South-West (SW) of the cluster center. Also in this case the data were obtained through the ESO/ST-ECF Science Archives and were pre-processed through the standard HST pipeline. We did not reduce the PC chip, since its small FOV ($\sim 40'' \times 40''$), combined with the extremely low stellar density at this distance from the cluster center ($\sim 4'$), sampled a very small number of objects, with no appreciable improvement to the general statistic. A map of the entire data-set and is shown in Figure 1.

2.1. Data reduction

The goal of this work is to obtain accurate photometry of MS stars down to the lowest mass allowed by the exposures. Since M 10 is a reasonably sparse GC ($c = 1.40^6$; Harris et al. (1996)) the images are not affected by severe crowding, even in the very central regions. The photometry of two data-sets was performed as follows. We used DAOPHOTII/ALLSTAR (Stetson 1987) to find stars, derive a spatially varying point spread function (PSF) and perform the first measurements for all stars in every single image. We then used DAOMATCH and DAOMASTER to match all stars in each chip, regardless of the filter, in order to find an accurate coordinate transformation between the frames. The matched solutions were then fed to MONTAGE2 in order to build a stacked image of each chip.

⁶ Central concentration, $c = \log(r_t/r_c)$

In this way we could eliminate all the cosmic rays and obtain an image of the stars with the highest signal-to-noise ratio. We ran the DAOPHOT/FIND routine and the PSF-fitting on the stacked image in order to obtain a deep master star list. The master list was then used as input for ALLFRAME (Stetson 1994), which simultaneously determines the brightness for stars in all frames while enforcing one set of centroids and one transformation between all images. Finally, all the magnitudes for each star were normalized to a reference frame and averaged together, and the photometric error was derived as the standard deviation of the repeated measures.

We note here that the presence of saturated stars in these deep images is the major source of artefacts causing spurious detections, especially in the core regions where most of the red giant stars are located. In order to clean our catalogues from false detections, we used a statistical approach similar to the one proposed by Cool et al. (1996), that employs the sharpness (sh) parameter provided as an output by ALLFRAME as the source quality diagnostic. By plotting sh as a function of the magnitude we found that spurious objects, detected around the haloes and along diffraction spikes of saturated stars, have sharpness values that differ from the ones representative of bona-fide stars, which typically have $-0.15 < sh < 0.15$. In Figure 2 we show that the effectiveness goodness of the selection in sharpness (left panel) in identifying false detections is confirmed by the fact that the objects with large sharpness values have also larger photometric errors (right panel).

We finally transformed the instrumental F606W (V) and F814W (I) magnitudes to the VEGAMAG system following the prescriptions of Sirianni et al. (2005) and Holtzman et al. (1995)⁷ for the ACS and WFPC2 samples, respectively. The relative star coordinates of both samples were transformed to the absolute right ascension and declination values (J2000) using the wide field catalogue published by Pollard et al. (2005) as secondary astrometric standard catalogue.

2.2. The color magnitude diagram

In Figure 3 we show the color–magnitude diagram (CMD) of the entire data set. The WFPC2 final catalogue (left panel) contains 4995 objects. The same data set have already been reduced by De Marchi & Paresce (1996) and later by Piotto & Zoccali (1999). By comparing our photometry with the CMD of the latter (see their Figure 1), no differences are evident. The consistency of the two photometric analyses is further confirmed by a direct comparison of their published luminosity function (LF; see Table 4) and the one calculated in this work for the WF2 chip (see Section 3 for a detailed discussion).

Due to the long exposure time of the WFPC2 images, the stars at the turn-off (TO) level in this data set are saturated. In order to obtain a CMD in the WFPC2 area with a I magnitude range comparable with that of the ACS data set, we decided to complement our observations with a V vs. $(V - I)$ ground based catalogue from Rosenberg et al. (2000)⁸. This data set was obtained using the 1.0 m Jacobus Kapteyn Telescope (JKT) at La Palma (Canary Island). We transformed the standard Johnson V, I magnitudes of the JKT catalogue to the WFPC2 VEGAMAG system adopting color term as derived

by comparison of all the non-saturated stars in the WFPC2 chips that were also measured in the ground-based images. No color term is necessary for the I band. The uncertainties in the V zero points and in the $(V - I)$ color transformations are of the order of 0.007 mag. Due to the extremely low crowding conditions of the area covered by the WFPC2 and to the relative proximity of M 10 ($R_{\text{sun}} = 4.4$ kpc; Harris 1996), the completeness of the ground based catalogue in this area is expected to be very high. By comparing the observed LFs from the WFPC2 and JKT data in the same area, we found a good agreement in the magnitude range $19 < I < 20$ (corresponding to the mass range of approximately $0.6M_{\odot} < M < 0.7M_{\odot}$). We therefore decided to use the JKT catalogue for stars with $I < 20$ and the WFPC2 catalogue at fainter magnitudes.

In the right panel of Figure 3 we show the CMD as derived from the photometric reduction of the ACS data set. The final catalogue contains 56812 objects. The MS of the cluster is clearly visible and well sampled well above the TO that occurs at $I \sim 17.5$. A population of candidate blue stragglers departing from the TO along a bright extension of the MS is also recognizable. For $I < 16$ saturation starts to occur, thus making the photometry of brighter stars unreliable.

According to Piotto & Zoccali (1999), due to the Galactic latitude of M 10 ($b = 23^{\circ}$), the contamination from foreground/background stars is small and should not effect the LF. On the other hand Pollard et al. (2005), using wide field imaging of evolved stellar populations, claim that field contamination, mainly from the Galactic disk, should be taken into account. Since no direct measurement of the field contamination in our magnitude range is possible, we used a statistical approach. A catalogue of stars using the Galactic model from Robin et al. (2003) covering an area of 1 square degree around the cluster center was used⁹. After scaling for the ACS and WFPC2 FOV, we found a contamination of 425 and 159 stars in our magnitude range respectively for each sample. This means that, even in the worst case of the WFPC2 sample, where the number of sources is small, field contamination would be of the order of $\sim 3\%$, and thus can be neglected.

The MS mean ridge lines for the two data sets (open circles in Figure 3) were computed by using a 2nd order polynomial to fit the locus of MS stars, after rejecting those farther than 2σ from the best fit line, where σ is the combined photometric uncertainty in V and I . Following De Marchi & Pulone (2007; hereafter DP07), we applied this same σ -clipping approach to identify the bona-fide stars to be used in computing the LF and MF of the cluster and, in order to increase the statistics, we decided to accept as bona-fide stars all those within 2.5σ of the ridge line of best fit. The catalogue obtained after this procedure, containing 46 407 and 4 390 stars respectively in the ACS and WFPC2 field, will be used hereafter to derive the LF and MF. We mark as shaded regions in the CMDs of Figure 3 the limits below which the photometric completeness, as detailed in Section 2.3, falls below 50%. All the stars in these region are not used for the LF and MF calculation.

The MS ridge line that we derived in this way agrees very well with the models of Baraffe et al. (1997). The level of agreement between the models and the observed data can be fully appreciated in Figure 3 where the models for metallicity $[M/H] = -1.3$ (dashed line) and $[M/H] = -1.0$ (solid line) are shown. As noted by DP07, the models of Baraffe et al. (1997) are calculated for the F606W and F814W filters of the WFPC2, which are slightly different from those on board the

⁷ Notice that we referred to Section 5.1 of WFPC2 Data Handbook for updated values of Photometric Zeropoints

⁸ The photometric catalogue can be retrieved at the web page <http://www.astro.unipd.it/globulars/>

⁹ <http://model.obs-besancon.fr/>

ACS. We used the same method proposed in their work in order to translate the filter from the WFPC2 to the ACS system. Briefly, by using synthetic model atmosphere from e.g. the ATLAS9 library of Kurucz (1993), it is possible to calculate the magnitude difference in the same filter for the two cameras as a function of the effective temperature of the star. As shown in Figure 3 the agreement of the translated model in the ACS sample (right panel) is very good. The best fit of the model to the fiducial line corresponds to metallicity $[M/H] = -1.0$, distance modulus $(m-M) = 14.21$ and color excess $E(B-V) = 0.26$. These values are in excellent agreement with those of Piotto & Zoccali (1999), namely $(m-M) = 14.20$ and $E(B-V) = 0.29$. The metallicity of the best fitting model, $[M/H] = -1.0$, is fully consistent with the value measured observationally by Carretta & Gratton (1997), namely $[Fe/H] = -1.41$, whereas those for $[M/H] = -1.3$ deviate in color in the lower part of the CMD, as already pointed out by Pollard et al. (2005). We used an isocrone calculated for an age of 10Gyr, the only available at the moment from Baraffe et al. (1997). It is clear from their Figure 3a that the age plays a minor when void effect in the range of masses considered in this work. In light of the good agreement between the observed ridge line and the models of Baraffe et al. (1997), we feel confident that we can use the latter to translate magnitudes into masses.

2.3. Photometric completeness

A crucial step in determining an accurate LF is the estimation of the photometric completeness of the data. Completeness corrections were determined via artificial star tests following the method discussed by Bellazzini et al. (2002). We first generated a catalogue of simulated stars with a V magnitude randomly extracted from a LF modeled to reproduce the observed LF in the V band. Then the I magnitude was assigned at each sampled V magnitude by interpolating the mean ridge line of the cluster (see Figure 3). The coordinates of the simulated stars were calculated in the coordinate system of the reference frame and then translated to each single image using the same matching solutions found in the data reduction phase (see Section 2.1).

It is crucial to avoid interference between the artificial stars, since in that case the output of the experiments would be biased by artificial crowding not present in the original frame. For this reason the frames were divided in a grid of cells of fixed width (~ 15 pixel, i.e. more than 5 times larger than the mean FWHM of the stars in the frames) and only one star was randomly placed in such a box in each artificial test run. The artificial stars were added to the real images using the DAOPHOT/ADDSTAR routine. The reduction process was repeated on the artificial images in exactly the same way as for the scientific ones and applying the same selection criteria described in Section 2.1. More than 100 000 stars were eventually simulated in each chip, for a total of more than 500,000 stars in the entire data set. The photometric completeness (f) was then calculated as the ratio of the number of stars recovered after the photometric reduction (N_{out}) and the number of simulated stars (N_{in}). f is expressed as a function of I magnitude.

Due to the strong gradient in stellar density from the center of the cluster outwards, there is a significant dependence of the photometric completeness with radial distance, even though M 10 is a reasonably sparse GC and the images do not suffer from dramatic crowding. Nevertheless, in order to take this radial effect into account, we divided the en-

tire FoV in 6 zones characterized by a similar completeness. In Figure 1 the black full circles show the regions numbered from 1 to 6. The innermost four regions are included in the ACS FOV and are concentric annuli all centered on the nominal cluster center. We notice here that the center used in this work has been determined from accurate star counts of resolved stars in the central regions of the cluster from archival WFPC2 imaging of M 10 (Prop. 6607, P.I. F. Ferraro), as explained in a forthcoming paper (Dalessandro et al. 2010; in preparation). The adopted center of gravity is $\alpha_{J2000} = 16^{\text{h}} 57^{\text{m}} 8^{\text{s}}.92$, $\delta_{J2000} = -4^{\circ} 05' 58.''07$, which is in full agreement with the one of Harris et al. (1996).

Region 5 includes both the WF3 and WF4 chips of the WFPC2, which cover an area of equal crowding condition at the same radial distance, whereas Region 6 corresponds to the whole WF2 chip. In Figure 4 we report the resulting photometric completeness of each of the six regions as a function of the I -band magnitude. It is important to notice that, even in the very central region of the cluster where saturation biases the completeness, artificial star tests show that we sample the MS stellar population of the cluster down to ~ 5 mag below the TO (see solid line in lower panel), with a completeness in excess of 50%.

3. THE LUMINOSITY AND MASS FUNCTION

In order to derive the LF, we selected from our bona-fide photometric catalogues all stars within each of the six regions mentioned above and sorted them as a function of the I -band magnitude. The resulting observed LFs (OLFs) are shown as full circles in Figure 5 and as filled circles after correction for photometric completeness. The observed and completeness-corrected LFs are also provided in Table 2. In Figure 5 we also show, as a dashed line, the LF published by Piotto & Zoccali (1999) in the WF2 frame, which appears in excellent agreement with ours.

The solid line shown in Figure 5 are the theoretical LFs (TLFs) obtained by multiplying a simple power-law mass function (MF) of the type $dN/dm \propto m^{\alpha}$ by the derivative of the mass–luminosity relationship of Baraffe et al. (1997) for $[M/H] = -1.0$. We have adopted a distance modulus $(m-M) = 14.21$ and a color excess $E(B-V) = 0.26$ as found in Section 2.2. The power-law indices that correspond to the best fitting models for the six regions, from Region 1 to Region 6, are respectively $\alpha = 0.7, 0.4, 0.1, -0.3, -0.6, -0.9$. With the notation used there, the Salpeter IMF would have $\alpha = -2.35$ and a positive index implies that the number of stars is decreasing with decreasing mass. The wide range of MF slope indices from the cluster core to $2.5 r_{\text{hm}}$ indicates that stars in M 10 have experienced the effects of mass segregation. Massive stars are much more segregated in the central regions where the index is positive. The MFs are almost flat in the intermediate regions with an inversion of the trend outside, where the number of low mass stars is increasing compared to the more massive ones. We address this issue more quantitatively in Section 4.

4. THE GLOBAL MASS FUNCTION

In order to further investigate the dynamical state of M 10, we used the approach developed by Gunn & Griffin (1979). We ran the multi-mass Michie–King (MK) code originally developed by Meylan (1987, 1988) and modified

TABLE 2

LUMINOSITY FUNCTIONS MEASURED IN EACH OF THE SIX REGIONS. FOR EACH REGION, THE TABLE GIVES, AS A FUNCTION OF THE m_{814} MAGNITUDE, THE NUMBER OF STARS PER HALF-MAGNITUDE BIN BEFORE (N_o) AND AFTER (N) COMPLETENESS CORRECTION AND THE UNCERTAINTY (σ_N) ON N .

m_{814}	Area 1			Area 2			Area 3			Area 4			Area 5			Area 6		
	N_o	N	σ_N	N_o	N	σ_N	N_o	N	σ_N	N_o	N	σ_N	N_o	N	σ_N	N_o	N	σ_N
17.25	121	131	24	259	271	30	269	279	27	511	517	32	28	28	7	10	10	4
17.75	195	207	31	414	434	37	497	511	37	948	961	45	55	55	10	10	10	4
18.25	253	285	38	491	519	41	564	584	39	1162	1181	49	74	74	12	24	24	6
18.75	298	325	40	570	610	44	719	744	45	1745	1788	63	113	113	16	29	29	7
19.25	299	342	40	647	709	48	763	805	46	1990	2047	69	156	164	18	35	35	8
19.75	219	263	33	632	700	47	796	850	47	2029	2103	68	183	192	19	43	46	9
20.25	213	262	33	551	640	44	730	791	45	2065	2162	68	218	232	21	56	61	10
20.75	206	276	35	540	638	44	691	776	44	2072	2202	69	213	231	21	52	56	10
21.25	165	249	35	488	608	44	730	840	48	2137	2320	73	293	322	26	69	75	11
21.75	155	257	37	492	660	48	846	1011	54	2673	2963	87	351	390	29	76	83	12
22.25	138	256	41	474	675	50	861	1062	57	3204	3624	101	459	520	33	143	160	18
22.75	—	—	—	363	553	46	657	866	52	2745	3188	94	451	526	33	135	152	16
23.25	—	—	—	247	437	43	424	613	43	1935	2345	76	333	404	27	112	127	14
23.75	—	—	—	—	—	—	241	417	37	1260	1667	65	256	319	23	81	93	12
24.25	—	—	—	—	—	—	—	—	—	814	1416	67	168	228	19	59	71	10
24.75	—	—	—	—	—	—	—	—	—	—	—	—	86	138	16	29	37	7
25.25	—	—	—	—	—	—	—	—	—	—	—	—	—	—	—	23	35	8

by Pulone et al. (1999), to assess whether the observed MF variations with radius are consistent with the degree of mass segregation expected from energy equipartition due to two-body relaxation. In short, every model run generates a power-law MF of variable index α characterized by four cluster structural parameters i.e. the core radius (r_c), the scale velocity (v_s), the central value of the dimensionless gravitational potential W_0 and the anisotropy radius (r_a). The first selection of the models is done by excluding all those regions in the parameter space that do not fit simultaneously the observed SBP and the central value of the velocity dispersion (σ_p).

The SBP used here was derived from accurate star counts obtained by combining a photometric catalogue sampling cluster stars in the central regions from WFPC2 high resolution images and multi-band wide field images from the Wide Field Imager (WFI) mounted on the MPI 2.2m telescope at La Silla (Chile), extending out to the tidal radius ($r_t = 21'48$; Harris et al. 1996). Details about the SBP can be found in Dalessandro et al. (2009, and references therein). As regards the velocity dispersion, the value of $\sigma_p = 6.60$ Km/s comes from McLaughlin & van der Marel (2005).

While forcing the MK model to reproduce the SBP and the observed value of the velocity dispersion will set some constraints on the cluster's structural parameters and on the range of indices of the MF, in order to find a unique solution the additional condition that the model LFs agree simultaneously with the OLFs at different radii must be imposed (see e.g. De Marchi et al. 2006; DP07). This sets very stringent constraints on the shape of the present global MF (GMF), i.e. the MF of the cluster as a whole.

We do so in Figure 6, where we compare the LFs (corrected for completeness, solid circles) with the theoretical MFs predicted by the MK model at the specific radial locations, folded through the M–L relationship, exactly as we did for the model power-law MFs in Figure 5. Here, however, the shape of the local MF is not free, but is completely set by the two-body relaxation process acting on the GMF, as per the MK model. The best fitting model also reproduces very well the SBP with a core radius $r_c = 50''4$ and a dimensionless central potential $W_0 = 7$, in excellent agreement with the values of $r_c = 49''41$

and $W_0 = 6.50$ from McLaughlin & van der Marel (2005).

The GMF index of the best fitting model is $\alpha = -0.7$ (as already mentioned in our formalism a Salpeter IMF would have $\alpha = -2.35$) in the range $0.25 - 0.8 M_\odot$. In the case of NGC 2298 (DP07) and NGC 6218 (De Marchi et al. 2006), an excellent match was found between the index of the GMF and that of the local MF as measured at the half mass radius. It is expected that the actual MF near the half mass radius should be only marginally affected by mass segregation and should thus be representative of the GMF of the cluster (see De Marchi et al. 2000, and references therein). It is interesting to note that also in the case of M 10 the index of the GMF ($\alpha = -0.7$) is in good agreement with the value $\alpha \sim -0.6$ (see Section 3) measured near the half mass radius ($r_{hm} = 124''$; see Section 5).

The good match between the observed LFs and those from the MK model suggests that, in its present state, M 10 is consistent with a condition of energy equipartition. On the other hand, since the MK approach provides by design a snapshot of the cluster evolution, it is not possible to infer from it the past dynamical history of the cluster, and in particular whether internal energy sources such as binary stars or an IMBH are playing any role in the evolution of M 10. However, this is possible using dynamical N-body models that incorporate single and binary star evolution; these will be discussed in the next section.

5. N-BODY SIMULATIONS

We use state-of-the-art direct N-body simulations to model the dynamics of M 10. They are based on NBODY6 (Aarseth 2003), modified as discussed in Trenti et al. (2007b) to improve accuracy in the presence of an IMBH. Interactions between particles are treated using regularization of close gravitational encounters with no softening. This choice is motivated by the need to realistically model the collisional dynamics within the sphere of influence of the IMBH. An in-depth discussion of the numerical simulations and the software used is found in Gill et al. (2008). We use the same set of runs presented in that paper, with the addition of further simulations containing primordial binary fractions equal

to 1%, 3% and 5%. These primordial binaries were assigned binding energies in the range from ϵ_{min} to $133\epsilon_{min}$, where $\epsilon_{min} = \langle m(0) \rangle \sigma_c(0)^2$, $\sigma_c(0)$ is the initial velocity dispersion, and $\langle m(0) \rangle$ the initial average mass of the system¹⁰. This choice makes our binaries hard, with separations typically lower than 10 AU. Binaries are likely to have a non-negligible impact on the results we obtain, so the addition of these runs is an important improvement over Pasquato et al. (2009). The masses of stars in binary systems have been selected independently according to the chosen IMF after the instantaneous step of stellar evolution has been applied to evolve the turn-off mass to $0.8 M_\odot$. We are essentially adopting a random pairing function (see Kouwenhoven et al. 2009). Binary exchange interactions are frequent, especially in the core of the system, so by $t \gtrsim 5t_{rh(0)}$ (when we consider the simulation snapshots for the analysis presented here) more than 50% of the binaries no longer have their initial companion. Hence the details of the pairing function are not expected to significantly affect the measured amount of mass segregation. The initial binary eccentricity distribution is thermal (see Trenti et al. 2008). For a typical velocity dispersion of 10 km/s, the binary binding-energy distribution corresponds to a semiaxis distribution $< 10AU$ (see Trenti et al. 2008, 2010). Binaries with larger separations would be quickly destroyed by three-body encounters (Heggie 1975) while binaries with larger binding energy (and smaller semiaxis) than those considered here are generally possible only if both components are compact remnants (otherwise their apocenter separation could be less than the physical radius of the stars for eccentric orbits). In any case such tightly bound objects are essentially dynamically inert (see Trenti et al. 2008, for runs that consider an extended binding energy range). Observations of nearby star forming regions and the Galactic field, find a primordial binary fraction which is usually quite high (Duquennoy & Mayor 1992; Kouwenhoven et al. 2005, 2007) but this refers to all binaries, independent of their binding energy. In our case only *hard* binaries are included in the primordial binary population, as softer binaries would be quickly destroyed by three-body interactions, having no long-term dynamical effect. This makes our choice of exploring the 0% – 10% range in primordial binary fraction justified.

Here we summarize the initial conditions to the various runs we use to explore a variety of different primordial configurations, changing the IMF to check that our conclusions are independent of the initial configuration, and the primordial binary fraction to study its influence on our conclusions. The initial distribution function is a single-mass King (1966) model, even though a fully realistic mass spectrum is then used in the N-body calculations. The number of particles is varied from $N = 1.6 \cdot 10^4$ to $N = 3.2 \cdot 10^4$. If we take the average mass of a GC star to be about $0.5M_\odot$, this numbers translate to roughly $8 \times 10^3 M_\odot$ and $1.6 \times 10^4 M_\odot$. Conversely the mass of M10 is estimated by McLaughlin & van der Marel (2005) to be $\approx 1.55 \times 10^5 M_\odot$.

None of our simulations includes primordial mass segregation, as all stars start out with the same distribution, regardless of mass. Recently, primordial mass segregation was proposed to explain the extreme depletion of the stellar mass functions observed in several GCs, which exceeds the predictions

of primordially non-segregated simulations (Baumgardt et al. 2008). Primordial mass segregation, in combination with an external tidal field, can be used to justify a much higher rate of depletion of low-mass stars. Moreover, Allison et al. (2009) find that primordial mass segregation naturally arises in clusters initialized in a clumpy, subvirial (dynamically cold) state. In the present work we do not explicitly include mass segregation in the initial conditions. However, in order to draw our conclusions on the presence of an IMBH we consider the mass segregation profiles of relaxed configurations only, by looking at times $t > 5t_h$. So it is the equilibrium value of mass segregation that matters for our argument, and we expect it not to be influenced by its primordial value, similarly to what is found for r_c/r_{hm} , which settles to an equilibrium value after several relaxation times, irrespective of its starting value (see Trenti et al. 2007c; Trenti et al. 2010).

Initial stellar masses come from either a Salpeter (1955) or Miller & Scalo (1979) IMF. We have adopted a lower limit to the IMF of $0.2M_\odot$ and an upper limit of $100M_\odot$ (prior to the stellar evolution step). The choice of the lower mass limit is driven by the mass of the faintest stars that are observable in our data set with a satisfactory completeness ($\approx 50\%$). Pasquato et al. (2009) computed control runs including stars with masses down to $0.1M_\odot$, obtaining the same results as in the case of runs with masses truncated at $0.2M_\odot$. Stellar evolution is carried out in a single step to a turn-off mass of $M_{T.O.} = 0.8M_\odot$, at the beginning of the simulation. The details and the motivation of this choice are explained by Gill et al. (2008). Half of the runs included in Pasquato et al. (2009), contained primordial binaries, with a binary fraction of 10%. This includes runs containing both an IMBH and a 10% binary fraction, which allow us to study the combined effect of the two ingredients. Qualitatively, the quenching effects of binaries and of an IMBH sum, leading to an enhanced depression of mass segregation. This fraction can reasonably be considered as the value representative of the binary fraction of a galactic globular cluster (see Bellazzini et al. 2002). In this paper, new simulations without an IMBH but with primordial binary fractions of 1%, 3% and 5% are considered. These new runs have a Miller & Scalo (1979) IMF and $3.2 \cdot 10^4$ particles. They are included to give a more fine-grained scale in binary fraction, to properly compare its dynamical effects with the observations.

In about half of the simulations, an IMBH with mass $M_{IMBH} \simeq 0.01$, or $\sim 1\%$ of the entire cluster is present. Values of the M_{IMBH}/M_{GC} in the range 0.5% to 2% are expected by extending the Magorrian et al. (1996) scaling law to GCs. As shown by Gill et al. (2008), even rising the mass of the IMBH up to 3% of the cluster mass does not change the amount of mass segregation found in the simulations. Gill et al. (2008) further suggest that, in general, the dependence of the quenching of mass segregation on IMBH mass is weak, given that the quenching mechanism is based on the scattering of stars by the binary system formed in the GC center by the IMBH and a massive companion (e.g. a stellar-mass black hole). The tidal field from the parent galaxy is taken into account in the simulations assuming circular orbits with the tidal cut-off radius self-consistent with the initial cluster concentration parameter. Dinescu et al. (1999) find that M10 has a moderately elliptic orbit around the galactic center, with eccentricity $e = 0.19 \pm 0.05$. This low value of eccentricity makes the circular orbits adopted in this work a satisfactory approximation to the orbit of M10. For further details of the tidal force treat-

¹⁰ The choice of the number 133 follows Heggie et al. (2006), where binary binding energies ranged from $3kT_c$ to $400kT_c$, with T_c defined as the central temperature of the system.

ment see Trenti et al. (2007c).

5.1. Comparison with the observations

We applied the same algorithm used by Pasquato et al. (2009) on NGC 2298 to the catalogue of stars we obtained for M 10, in order to produce a radial mass segregation profile. A half-mass radius was obtained for main sequence stars (with masses ranging from 0.26 to $0.8 M_{\odot}$), by computing their total mass within the radial range covered by the observations and finding the radius which contains half of it in projection. A non-parametric mass growth-curve was constructed via spline interpolation as in Pasquato et al. (2009). We obtain $r_{hm} = 124''$, which is slightly larger than the half-light value of $108.6''$ determined by Harris et al. (1996). This is not surprising and is per se an indication of mass segregation, since bright giants (with masses around the turn-off mass) dominate the luminosity profile. We used the obtained half-mass radius to normalize our mass-segregation indicator, i.e. the mean mass of MS stars as a function of radius, following Pasquato et al. (2009). The mass segregation profile $\Delta m(r)$ is constructed by plotting the mean mass of a main-sequence star (normalized by subtracting its value at the half light radius) as a function of radius.

We compared the observational mass segregation profile to the confidence intervals predicted by means of the set of simulations used in Pasquato et al. (2009) with the addition of the three new IMBH-free runs with a 1%, 3%, and 5% primordial binary fraction, consistently defining the range of observable MS stars from 0.26 to $0.8 M_{\odot}$. Gill et al. (2008) show that the simulations reach a stationary configuration with respect to mass segregation after approximately 5 relaxation times. For the sake of comparing them to the observed mass segregation profile of M 10, the simulations were analyzed between 7 and 9 initial-half-mass relaxation times.

Figure 7 (left panel) shows the M 10 mass segregation profile (red line) superimposed to the green and blue shaded areas corresponding to the 2σ confidence regions defined by the simulations without an IMBH and with an IMBH of mass 1% of the total cluster mass respectively. The observational profile lies within the superposition of the two shaded areas. Therefore, while it is possible that an IMBH is lurking in the center of M 10, we cannot rule out alternative explanations. In particular, the lower envelope of the green shaded area is defined, towards the center, by runs containing primordial binaries with an initial binary fraction of 10%. This is expected, because binaries act as an energy source capable of halting core collapse, as shown by Trenti et al. (2007b,c) and consequently can partially mimic the behavior of an IMBH, so they give rise to a shallower profile with respect to runs containing only single stars. The right panel of Figure 7 shows the same plot of the left one, where only the 32k-particle simulations with no primordial binaries were included (binaries do form dynamically in these runs, but only in small numbers). In this case the data would be incompatible with the no-IMBH scenario, and we would conclude that an IMBH is likely present in the core of M 10.

The two plots described above clearly show the crucial role played by binary stars in the dynamical evolution of the cluster. In order to investigate in more detail the effect of the binary fraction in the predictive capability of our model, we compare the observed mass segregation profile of M 10 with the prediction of the 32k-particle IMBH-free simulations with 3% and 5% primordial binary fraction (respectively left and right panel in Figure 8). It is apparent that these simulations

can reproduce the observations fairly well, i.e. that in the absence of an IMBH a binary fraction in this range is required to explain the observations of mass segregation in M 10.

We therefore conclude that a precise measurement of the MS binary fraction in M 10 would allow us to reach a firmer conclusion on the presence of an IMBH. A dynamically significant fraction of binaries is a viable alternative to the IMBH hypothesis for explaining the observed mass segregation profile, since both can be active energy sources capable of halting core collapse and quenching mass segregation.

6. SUMMARY AND CONCLUSIONS

In this work we present a study of the dynamical state of the globular cluster M 10 through the characterization of the radial properties of its stellar LF and MF. We used a combination of archival deep ACS and WFPC2 images to sample cluster stars from the core regions through to $\sim 2.5 r_h$ in the mass range $0.25 - 0.8 M_{\odot}$. The full data set was divided in six regions at different distances from the cluster center and characterized by the same photometric completeness. The LF was calculated for each region and converted to a MF using the mass-luminosity relationship of Baraffe et al. (1997) for the metallicity of the cluster. Each of the local MFs was fitted using a simple power law of the type $dN/dm \propto m^{\alpha}$ and the best fitting indices were found to be $\alpha = 0.7, 0.4, 0.1, -0.3, -0.6, -0.9$ from the center outwards. A positive value of α means that the number of stars decreases with decreasing mass. This radial change in the MF index is a clear sign of mass segregation in M 10. To better characterize this effect, we built a multi-mass Michie-King model to reproduce the observed radial variation of the MF and the cluster's SBP and velocity dispersion and found that the distribution of the stars in the cluster is compatible with a condition of equipartition of energy. The GMF as obtained by the Michie-King model is a power-law with index $\alpha = -0.7$, in agreement with the value $\alpha \sim -0.6$ near the half mass radius ($r_{hm} = 124''$).

In order to investigate in more detail the dynamical history of M 10, we used N-body simulations that include the presence and evolution of binaries, with the goal to understand whether the current mass segregation profile requires the presence of an IMBH. Within the current uncertainties, we cannot exclude an IMBH of mass $\sim 1\%$ of the total cluster mass, although a plausible alternative explanation of the observed mass segregation profile is the presence of a substantial amount of binaries, likely primordial in origin, capable of significant dynamical effects. We show that N-body simulations initialized with a primordial binary fraction in the range of 3–5% are effectively able to correctly predict the observed mass segregation profile of M 10.

M 10 is a better candidate than NGC 2298 for an observational follow-up aimed at detecting an IMBH. While the latter cluster does not contain an IMBH according to Pasquato et al. (2009), M 10 shows a shallow mass segregation profile which could be interpreted as the fingerprint of an IMBH. The comparison of the observed mass segregation with the simulations clearly demonstrates that the cluster binary stars play a key role in defining its dynamical state and therefore cannot be ignored. The binary fraction of the cluster needs to be better constrained.

We thank the anonymous referee for the useful suggestions and comments that helped to significantly improve the overall quality of the paper. Part of this research was carried out

while Giacomo Beccari, Mario Pasquato, Guido De Marchi and Michele Trenti were participating to the Kavli Institute for Theoretical Physics (UCSB, Santa Barbara, California) program on "Formation and evolution of Globular Clusters". Support for grant HST-AR-11284 was provided by NASA

through a grant from STScI, which is operated by AURA, Inc., under NASA contract NAS 5-26555. This work was supported in part through NASA ATFP grant NNX08AH29G and by the National Science Foundation under Grant No. PHY05-51164.

Facilities: HST (ACS), JKT.

REFERENCES

- Aarseth, S. J. 2003, *Gravitational N-Body Simulations*, by Sverre J. Aarseth, pp. 430. ISBN 0521432723. Cambridge, UK: Cambridge University Press, November 2003
- Allison, R. J., Goodwin, S. P., Parker, R. J., de Grijs, R., Portegies Zwart, S. F., & Kouwenhoven, M. B. N. 2009, *ApJ*, 700, L99
- Anderson, J., & van der Marel, R. P. 2009, arXiv:0905.0627
- Baraffe, I., Chabrier, G., Allard, F., & Hauschildt, P. H. 1997, *A&A*, 327, 1054
- Baumgardt, H., Hut, P., Makino, J., McMillan, S., & Portegies Zwart, S. 2003a, *ApJ*, 582, L21
- Baumgardt, H., Makino, J., Hut, P., McMillan, S., & Portegies Zwart, S. 2003b, *ApJ*, 589, L25
- Baumgardt, H., Makino, J., & Ebisuzaki, T. 2004, *ApJ*, 613, 1143
- Baumgardt, H., Makino, J., & Hut, P. 2005, *ApJ*, 620, 238
- Baumgardt, H., De Marchi, G., & Kroupa, P. 2008, *ApJ*, 685, 247
- Bellazzini, M., Fusi Pecci, F., Messineo, M., Monaco, L., & Rood, R. T. 2002, *AJ*, 123, 1509
- Dallessandro, E., Beccari, G., Lanzoni, B., Ferraro, F. R., Schiavon, R., & Rood, R. T. 2009, *ApJS*, 182, 509
- Duquennoy, A., & Mayor, M. 1992, *Binaries as tracers of star formation. Proceedings.*, by Duquennoy, A.; Mayor, M.. Cambridge University Press, Cambridge (UK), 1992, 301 p., ISBN 0-521-43358-4
- Carretta, E., & Gratton, R. G. 1997, *A&AS*, 121, 95
- Chakrabarty, D. 2006, *AJ*, 131, 2561
- Cool, A. M., Piotto, G., & King, I. R. 1996, *ApJ*, 468, 655
- De Marchi, G., & Paresce, F. 1996, *Science with the Hubble Space Telescope - II*, 310
- De Marchi, G., Paresce, F., & Pulone, L. 2000, *ApJ*, 530, 342
- De Marchi, G., & Pulone, L. 2007, *A&A*, 467, 107
- Dinescu, D. I., Girard, T. M., & van Altena, W. F. 1999, *AJ*, 117, 1792
- Farrell, S. A., Webb, N. A., Barret, D., Godet, O., & Rodrigues, J. M. 2009, *Nature*, 460, 73
- Ferraro, F. R. 2006, arXiv:astro-ph/0601217
- Gebhardt, K., Rich, R. M., & Ho, L. C. 2005, *ApJ*, 634, 1093
- Gebhardt, K., Rich, R. M., & Ho, L. C. 2002, *ApJ*, 578, L41
- Gill, M., Trenti, M., Miller, M. C., van der Marel, R., Hamilton, D., & Stiavelli, M. 2008, *ApJ*, 686, 303
- Gunn, J. E., & Griffin, R. F. 1979, *AJ*, 84, 752
- Harris, W. 1996, *AJ* 112, 1487 (revision 2003)
- Heggie, D. C. 1975, *MNRAS*, 173, 729
- Heggie, D. C., Trenti, M., & Hut, P. 2006, *MNRAS*, 368, 677
- Heggie, D. C., Hut, P., Mineshige, S., Makino, J., & Baumgardt, H. 2007, *PASJ*, 59, L11
- Holtzman, J. A., et al. 1995, *PASP*, 107, 156
- Hurley, J. R., Pols, O. R., & Tout, C. A. 2000, *MNRAS*, 315, 543
- Ibata, R., et al. 2009, *ApJ*, 699, L169
- King, I. R. 1966, *AJ*, 71, 64
- Kouwenhoven, M. B. N., Brown, A. G. A., Zinnecker, H., Kaper, L., & Portegies Zwart, S. F. 2005, *A&A*, 430, 137
- Kouwenhoven, M. B. N., Brown, A. G. A., Portegies Zwart, S. F., & Kaper, L. 2007, *A&A*, 474, 77
- Kouwenhoven, M. B. N., Brown, A. G. A., Goodwin, S. P., Portegies Zwart, S. F., & Kaper, L. 2009, *A&A*, 493, 979
- Kurucz, R. L. 1993, *IAU Colloq. 138: Peculiar versus Normal Phenomena in A-type and Related Stars*, 44, 87
- Lanzoni, B., Dallessandro, E., Ferraro, F. R., Miocchi, P., Valenti, E., & Rood, R. T. 2007, *ApJ*, 668, L139
- Mackey, A. D., Wilkinson, M. I., Davies, M. B., & Gilmore, G. F. 2008, *MNRAS*, 386, 65
- Madau, P., & Rees, M. J. 2001, *ApJ*, 551, L27
- Magorrian, J., Tremaine, S., Gebhardt, K., Richstone, D., & Faber, S. 1996, *Bulletin of the American Astronomical Society*, 28, 1423
- McLaughlin, D. E., & van der Marel, R. P. 2005, *ApJS*, 161, 304
- Meylan, G. 1987, *A&A*, 184, 144
- Meylan, G. 1988, *A&A*, 191, 215
- Miller, G. E., & Scalo, J. M. 1979, *ApJS*, 41, 513
- Miller, M. C., & Hamilton, D. P. 2002, *ApJ*, 576, 894
- Milone, A. P., Piotto, G., Bedin, L. R., & Sarajedini, A. 2008, *Memorie della Societa Astronomica Italiana*, 79, 623
- Noyola, E., & Gebhardt, K. 2006, *AJ*, 132, 447
- Noyola, E., & Gebhardt, K. 2007, *AJ*, 134, 912
- Noyola, E., Gebhardt, K., & Bergmann, M. 2008, *ApJ*, 676, 1008
- Pasquato, M., & Bertin, G. 2008, *A&A*, 489, 1079
- Pasquato, M., Trenti, M., De Marchi, G., Gill, M., Hamilton, D. P., Miller, M. C., Stiavelli, M., & van der Marel, R. P. 2009, arXiv:0904.3326
- Piotto, G., & Zoccali, M. 1999, *A&A*, 345, 485
- Pollard, D. L., Sandquist, E. L., Hargis, J. R., & Bolte, M. 2005, *ApJ*, 628, 729
- Portegies Zwart, S. F., Baumgardt, H., Hut, P., Makino, J., & McMillan, S. L. W. 2004, *Nature*, 428, 724
- Pulone, L., De Marchi, G., & Paresce, F. 1999, *A&A*, 342, 440
- Robin, A. C., Reylé, C., Derrière, S., & Picaud, S. 2003, *A&A*, 409, 523
- Rosenberg, A., Aparicio, A., Saviane, I., & Piotto, G. 2000, *A&AS*, 145, 451
- Salaris, M., & Weiss, A. 2002, *A&A*, 388, 492
- Salpeter, E. E. 1955, *ApJ*, 121, 161
- Sirianni, M., et al. 2005, *PASP*, 117, 1049
- Sollima, A., Beccari, G., Ferraro, F. R., Fusi Pecci, F., & Sarajedini, A. 2007, *MNRAS*, 380, 781
- Sollima, A., Bellazzini, M., Smart, R. L., Correnti, M., Pancino, E., Ferraro, F. R., & Romano, D. 2009, *MNRAS*, 396, 2183
- Spitzer, L. 1987, Princeton, NJ, Princeton University Press, 1987, 191 p.
- Stetson, P. B. 1987, *PASP*, 99, 191
- Stetson, P. B. 1994, *PASP*, 106, 250
- Trenti, M., & Stiavelli, M. 2007, *ApJ*, 667, 38 (a)
- Trenti, M., Ardi, E., Mineshige, S., & Hut, P. 2007, *MNRAS*, 374, 857 (b)
- Trenti, M., Heggie, D. C., & Hut, P. 2007, *MNRAS*, 374, 344 (c)
- Trenti, M., Ransom, S., Hut, P., & Heggie, D. C. 2008, *MNRAS*, 387, 815
- Trenti, M., Vesperini, E., & Pasquato, M. 2010, *ApJ*, 708, 1598
- van den Bosch, R., de Zeeuw, T., Gebhardt, K., Noyola, E., & van de Ven, G. 2006, *ApJ*, 641, 852
- Vesperini, E., & Chernoff, D. F. 1994, *ApJ*, 431, 231

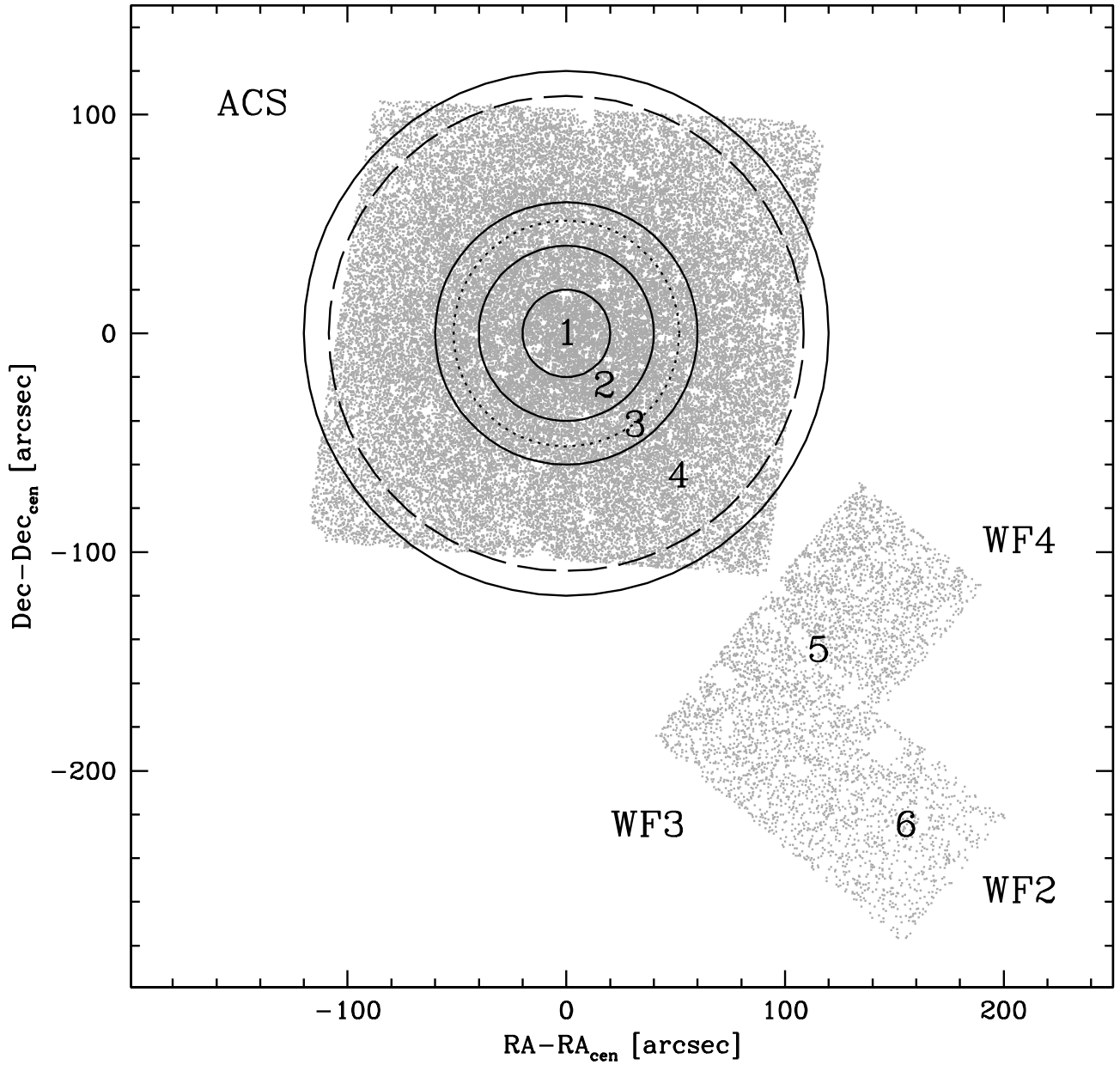


FIG. 1.— Map of the entire HST data-set used in this work. The position of each camera is labeled. The nominal core radius ($r_c = 0.86'$) and half mass radius ($r_h = 1.81'$) taken from Harris et al. (1996) are shown with dotted and dashed circles respectively. The full circles define the four annuli in which we divided the ACS photometry. For details on the radial division criteria of ACS and WFPC2 see Section 2.3

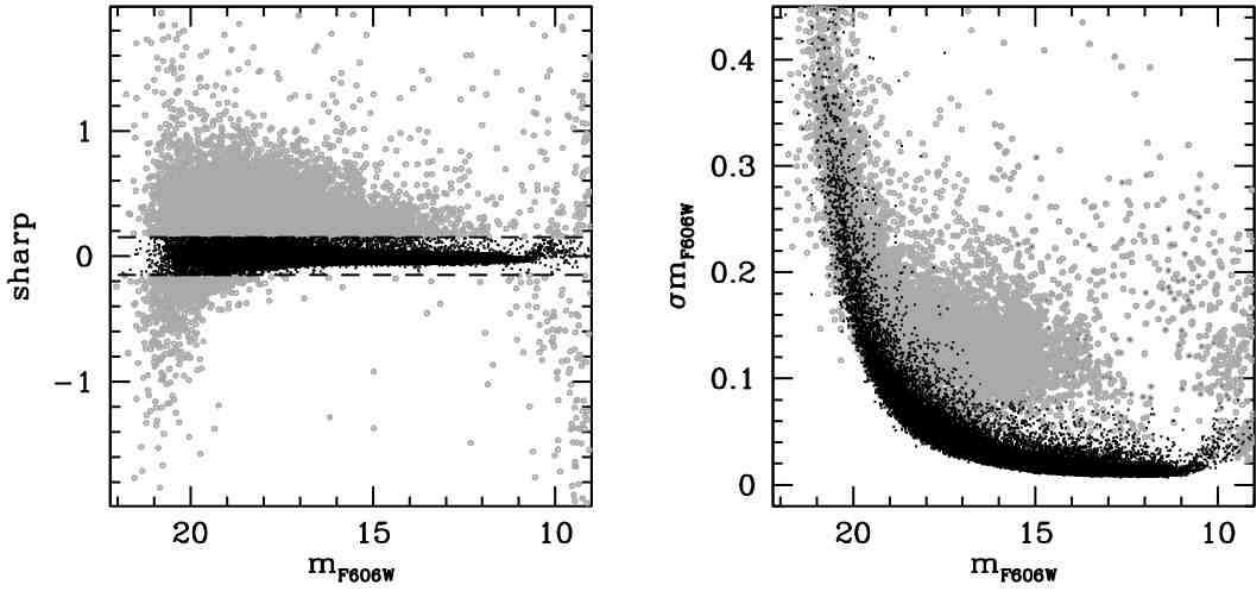


FIG. 2.— The sharpness (sh) parameter provided as an output by ALLFRAME is used as the source quality diagnostic. By plotting sh as a function of the magnitude (left panel) we found that spurious objects, detected around the haloes and along diffraction spikes of saturated stars, have sharpness values that differ from the ones representative of bona-fide stars ($-0.15 < sh < 0.15$). The goodness of the selection in sharpness in identifying false detections is confirmed by the fact that the objects with large sh values have also larger photometric errors (right panel; see Section 2.1 for details).

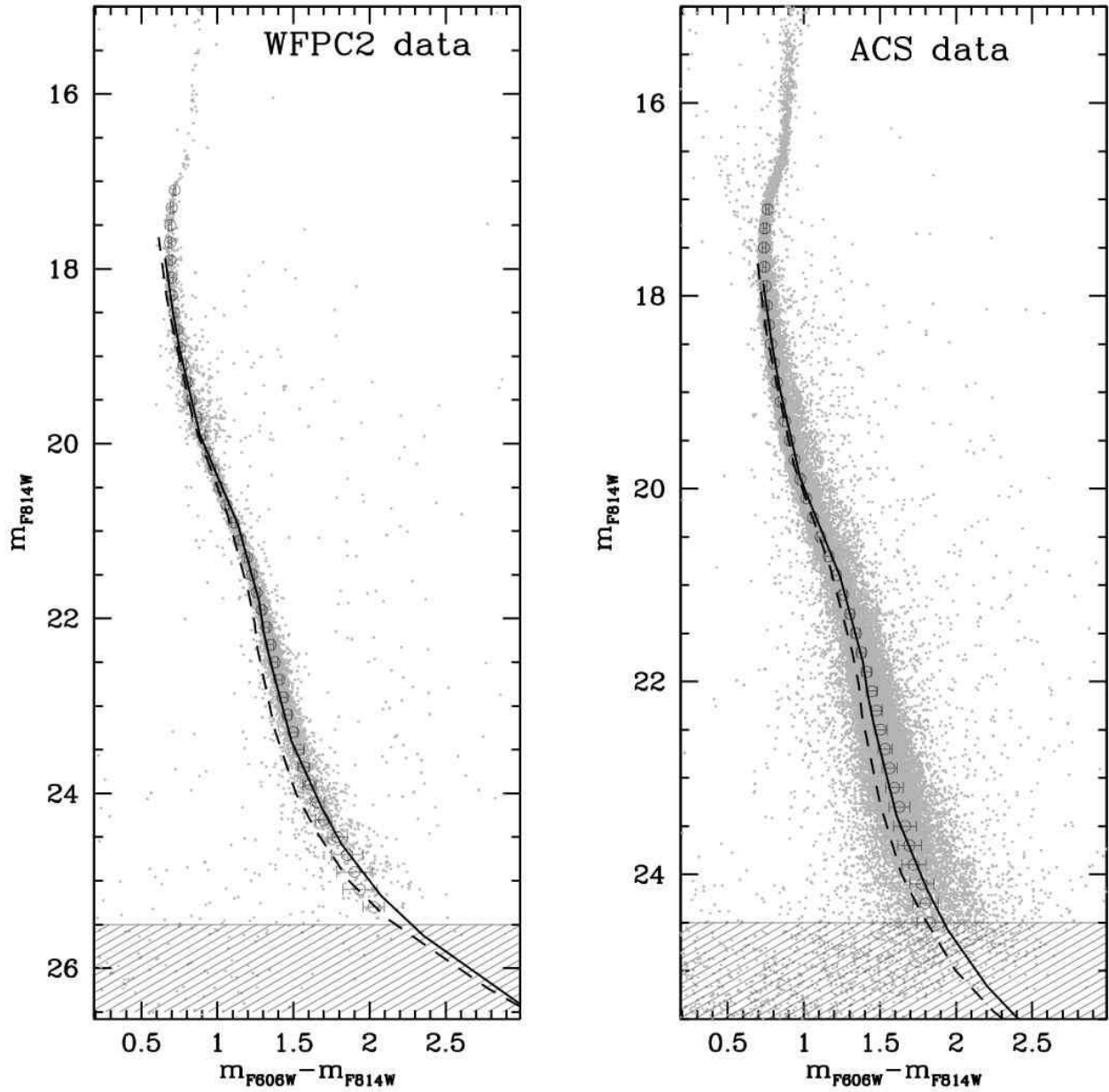


FIG. 3.— Color magnitude diagram of the cluster as obtained from photometric reduction of the WFPC2 (left panel) and ACS (right panel) data sets. The mean ridge line as obtained from 2 sigma rejection fitting process along the MS of each catalogue is also showed (open circles). Comparison between the observations and models by Baraffe et al. (1997) for $[M/H]=-1.3$ (dashed line) and $[M/H]=-1.0$ (full line) is also showed. The shaded regions in the CMDs show the limits within which the photometric completeness falls below 50% (see Section 2.3 for details).

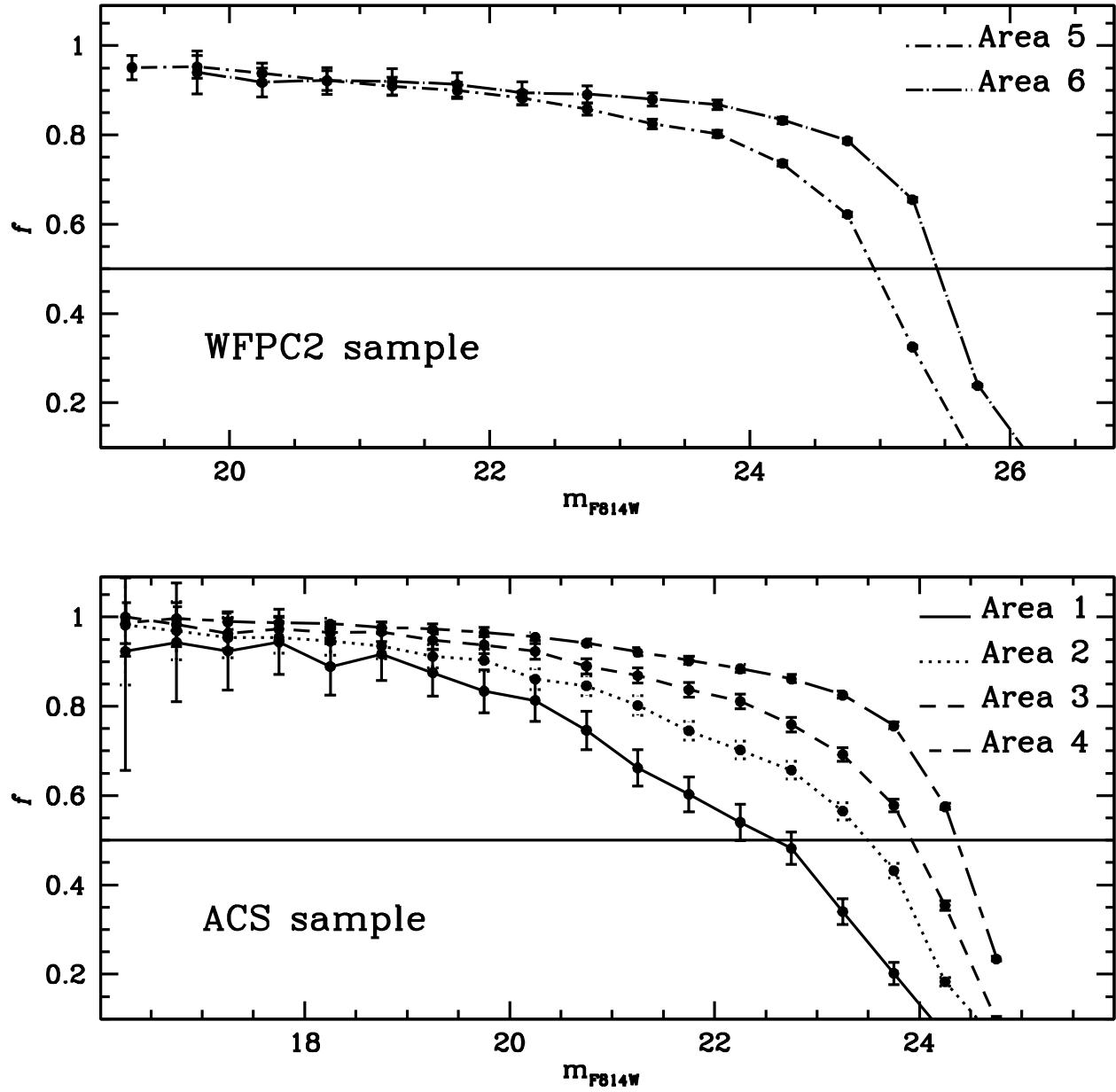


FIG. 4.— Photometric completeness f as a function of I for the two data sets. The ACS and WFC2 FoV have been divided in 4 and 2 area of same completeness respectively. The full horizontal line show the limits of 50% of completeness.

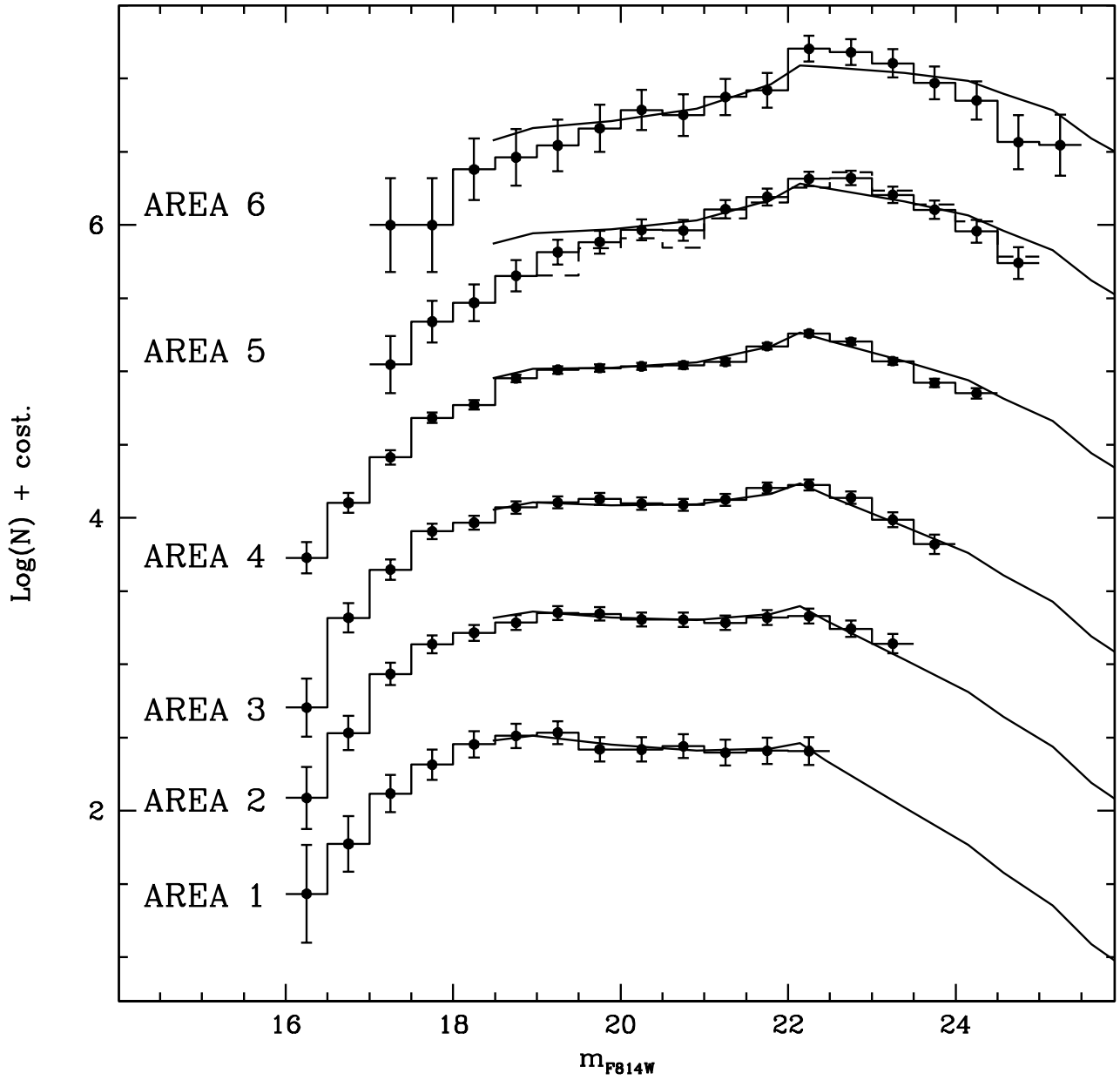


FIG. 5.— m_{F814W} OLFs of M 10, divided in different areas (see Section 3). The measurement as reported in Table 2 (full circles in the plot) are shifted by an arbitrary amount to make the plot more readable. The theoretical LFs that best fit the data are shown as solid lines. The index of their corresponding power-law MF is, from bottom to top, $\alpha = 0.7, 0.4, 0.1, -0.3, -0.6, -0.9$. A positive index means that the number of stars decreases with mass. All but the innermost LF reach a mass of $0.2M_{\odot}$.

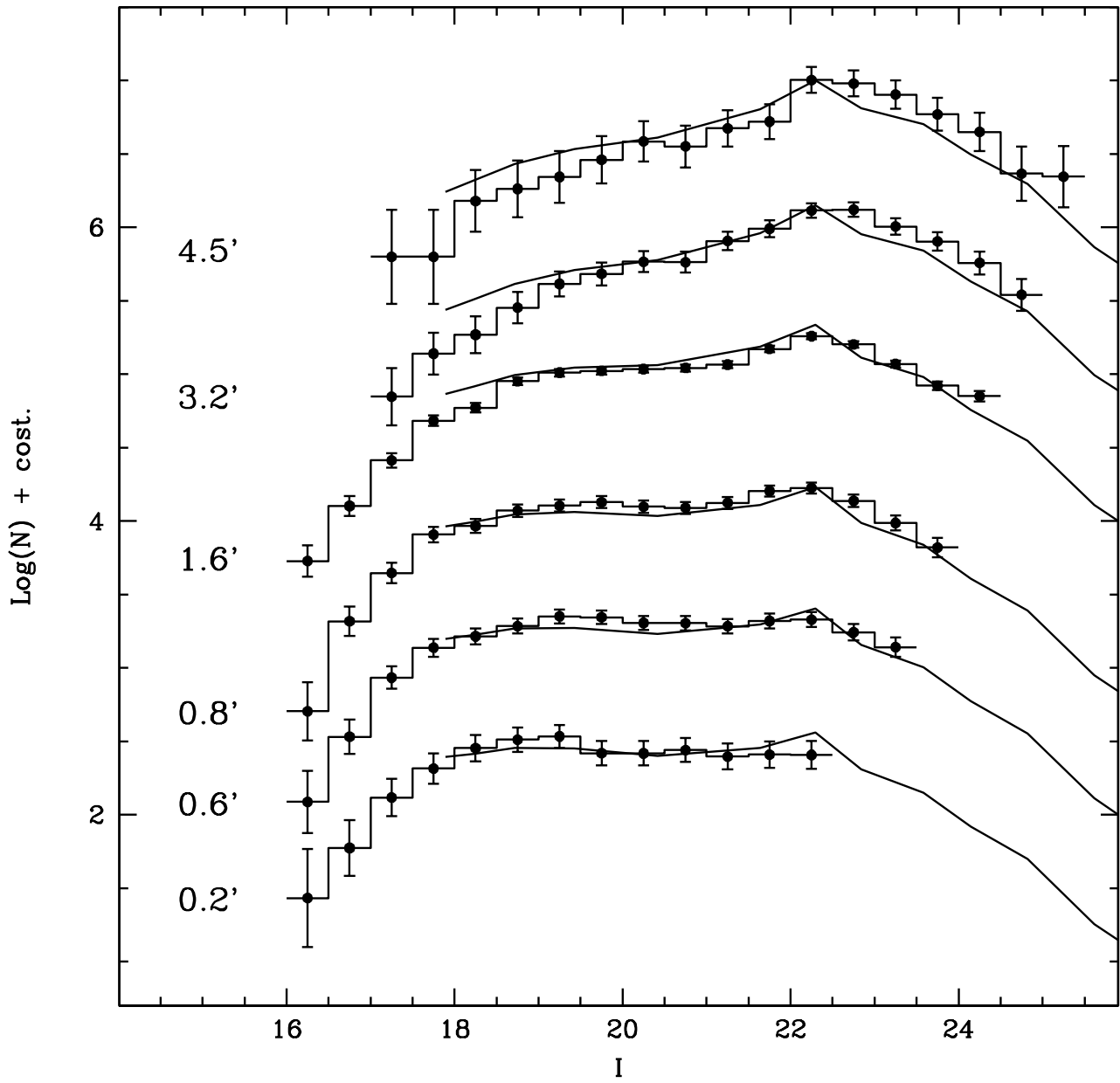


FIG. 6.— The LFs of Figure 5 (full circles) are compared with those predicted by our multi-mass Muchie-King model at various radii (reported left of the respective LF) inside the cluster (full line), for a GMF with fixed $\alpha = -0.7$. The predicted radial variation of the LF is fully consistent with the observations.

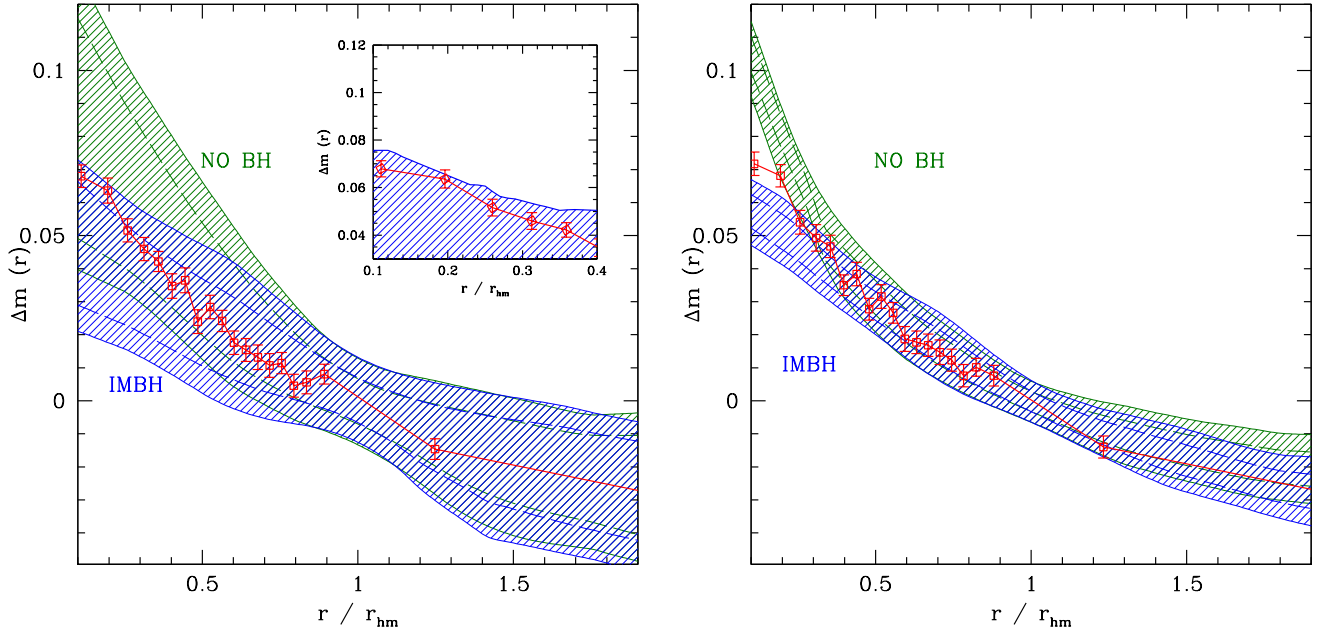


FIG. 7.— Observed radial mass segregation profile ($\Delta m(r)$ measured in M_{\odot}) for M 10 (red points with 1σ error bars), compared to expectations from numerical simulations. The shaded areas in both panels represent the 2σ confidence area for our simulations with an IMBH (blue) and without an IMBH (green). The long dashed lines define the 1σ confidence regions. The small inset shows the upper envelope of all snapshots of the simulations including an IMBH in the set. On the left panel the simulations contains runs with up to 10% primordial binaries as in Pasquato et al. (2009). On the right panel only the simulations with Miller & Scalo IMF, 32k particles and no primordial binaries are used. Binaries widen the confidence intervals towards low mass segregation values, thereby preventing a firm conclusion as to the presence of an IMBH (see Section 5.1).

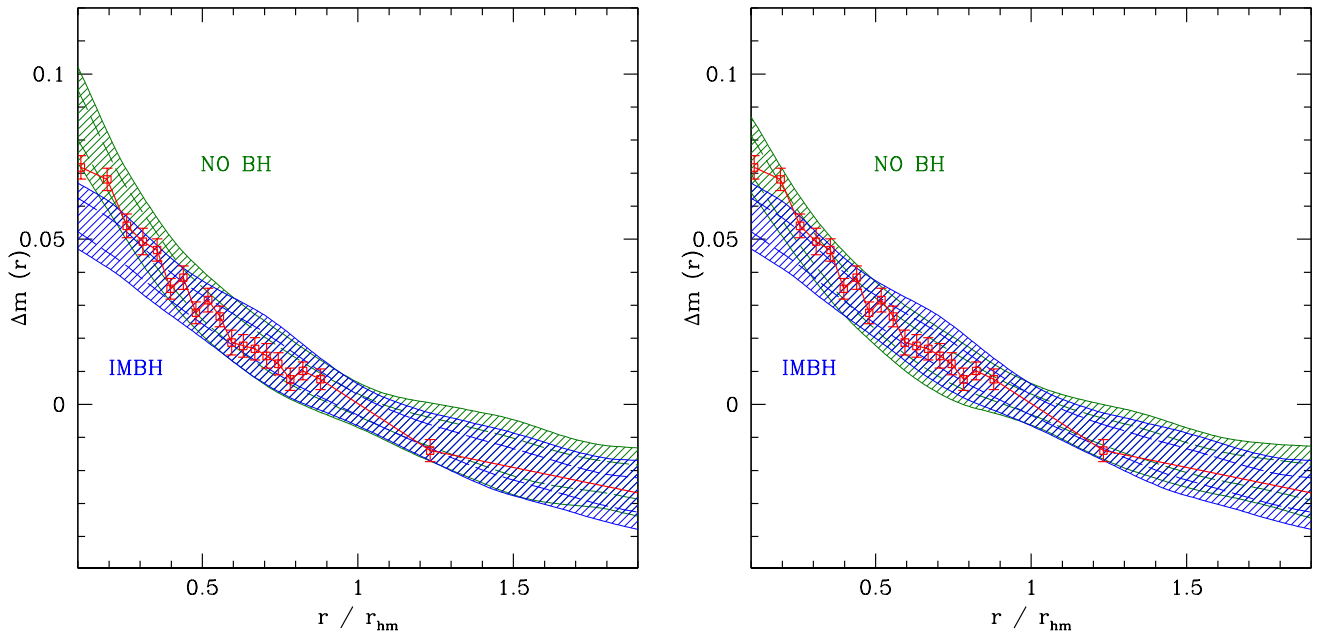


FIG. 8.— the same kind of plot as shown on Figure 7. Here we included simulation with a 3% and 5% of binaries on the left and right panel respectively.